Hybrid Helical Magnetic Microrobots Obtained by 3D Template-Assisted Electrodeposition

Muhammad A. Zeeshan,* Roman Grisch, Eva Pellicer, Kartik M. Sivaraman, Kathrin E. Peyer, Jordi Sort, Berna Özkale, Mahmut S. Sakar, Bradley J. Nelson, and Salvador Pané*

The development of micro- and nanoelectromechanical systems (MEMS/NEMS) technology has resulted in the fabrication of micro- and nanomachines that can be controlled wirelessly in liquid environments. Among the various actuation and control strategies for these machines, magnetic manipulation has emerged as the most versatile approach, and controlled manipulation of three-dimensional (3D) micromachines using magnetic field gradients, resonant magnetic fields and rotating magnetic fields has been demonstrated.[1–9] Rotation is a fundamental motion in biological systems at the micro and nano levels. Rotary motors are responsible for the motion of the bacterial flagella and the ATP synthase molecule. These motors convert rotational motion into translational motion, a strategy that has proven to be effective in the low Reynolds number regime.[10] Based on this principle, helical micromachines known as artificial bacterial flagella (ABFs) have been wirelessly manipulated in liquid environments using rotating magnetic fields.[3,4,11] Potential in vitro applications of these machines have made use of their ability to perform non-contact capture and transport of micro objects. For in vivo applications such as targeted drug delivery applications, it is foreseen that a group of these micro machines could have access to many hard-to-reach locations in the body and maximize drug loading and release. They could navigate through the circulatory, urinary and central nervous systems. The microrobots could also be applied in water remediation to patrol stagnant and flowing

wastewaters for effective degradation of organic pollutants. For this application, the microrobots should be functionalized with a photocatalytic compound. In any case a swarm control strategy will necessitate the development of reliable processes to fabricate these machines from a combination of materials that enable magnetic control and the incorporation of therapeutic molecules.

In combination with photolithography, electrodeposition has been used to fabricate relatively complex wirelessly controllable 3D micromachines.[12] Electrodeposition enables the synthesis of a wide variety of magnetic alloys, and allows the tuning of their properties by modulating factors such as the pH and temperature of the electrolytic bath, additives, and the current density or overpotential of deposition. Electrodeposition also enables the polymerization of a unique class of intrinsically conductive polymers (ICP) on metallic substrates. Among ICP, poly(pyrrole) (PPy) is the most widely studied and characterized due to its excellent biocompatibility, enhanced physical and chemical stability, the tunability of its surface towards various cell types, and the ability to incorporate therapeutic molecules into its matrix.[13,14]

In this paper, we describe a high throughput method to fabricate hybrid artificial bacterial flagella (h-ABFs) consisting of a ferromagnetic alloy head and a helical polymer tail (see **Figure 1**(a)). h-ABFs present a number of advantages compared to fully metallic specimens including a lighter weight that reduces sedimentation and facilitates navigation and better biocompatibility because of the replacement of metallic parts with PPy. The h-ABFs were synthesized by template-assisted two-step electrodeposition. The direct laser writing (DLW) process provided a simple method to make 3D photoresist templates acting as masks during the electrodeposition. With the use of a positive-tone photoresist, it is possible to make 3D cavities that can be filled by electrodeposition.[15] The hollow cavities were filled with magnetic cobalt-nickel (CoNi) and biocompatible PPy through electrodeposition. h-ABFs were physically stable in an aqueous environment with a rigid connection between the metallic and polymer segments. The wireless manipulation of these h-ABFs using rotating magnetic fields was demonstrated with a focus on swarm control.

An h-ABF is illustrated in Figure 1(a) and is designed to have a ferromagnetic head for magnetic actuation and a helical tail that provides propulsion in liquid environments.

M. A. Zeeshan, R. Grisch, K. M. Sivaraman, K. E. Peyer, B. Özkale, Dr. M. S. Sakar, Prof. B. J. Nelson, Dr. S. Pané Institute of Robotics & Intelligent Systems (IRIS) ETH Zürich, Zurich, Switzerland E-mail: marifzee@ethz.ch; vidalp@ethz.ch

Dr. E. Pellicer Departament de Física, Facultat de Ciències Universitat Autònoma de Barcelona Bellaterra, Spain

Prof. J. Sort Institució Catalana de Recerca i Estudis Avançats (ICREA) and Departament de Física Universitat Autònoma de Barcelona Bellaterra, Spain

© 2013 Wiley-VCH Verlag GmbH & Co. KGaA, Weinheim
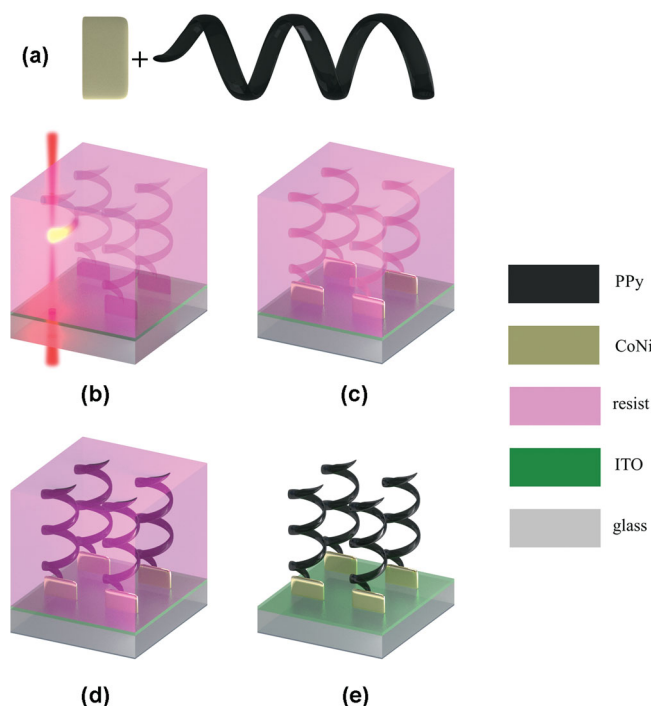
Figure 1. Processing steps for obtaining h-ABFs: (a) Illustration of the hybrid structure consisting of CoNi "head" and PPy "tail", (b) the 3D templates are written into the positive-tone AZ 9260 photoresist by Nanoscribe. (c) After development, CoNi heads were electrodeposited by pulse electrodeposition. (d) The PPy helical tail was obtained after the electropolymerization of pyrrole. (e) An array of h-ABFs is obtained after the removal of the resist with acetone.

Figure 1(b) to (e) schematically shows the processing step. The sample consists of a transparent indium tin oxide (ITO) electrode layer and a positive-tone photoresist layer deposited on a glass substrate. The ITO layer acts as a working electrode (WE) in the electrochemical cell, while the unexposed regions of the photoresist provide a mask for electrodeposition. During the DLW process, the photoresist is exposed by the laser from the back side of the glass. During exposure the beam passes through the ITO layer. Therefore, it is necessary for the ITO layer to be optically transparent. A 95% transparency was achieved at a laser wavelength of 780 nm after annealing (see Figure S1.1). After the spin coating process, the 3D template was written by focusing the laser into the resist while moving the sample with a piezo-stage in three dimensions and subsequent development (Figure 1(b)). Figure 1(c) and (d) show the two electrodeposition steps used to fill the channels into the photoresist template with CoNi and PPy, respectively. The h-ABFs were released by dissolving the photoresist with the acetone. The h-ABFs with a minimal feature size of 650 nm and a total length of 20 μm were achieved by this process. To investigate the swimming efficiency, two different designs were developed which vary in the diameter of the helical tail (see Figure S2.1 and Table S2.1).
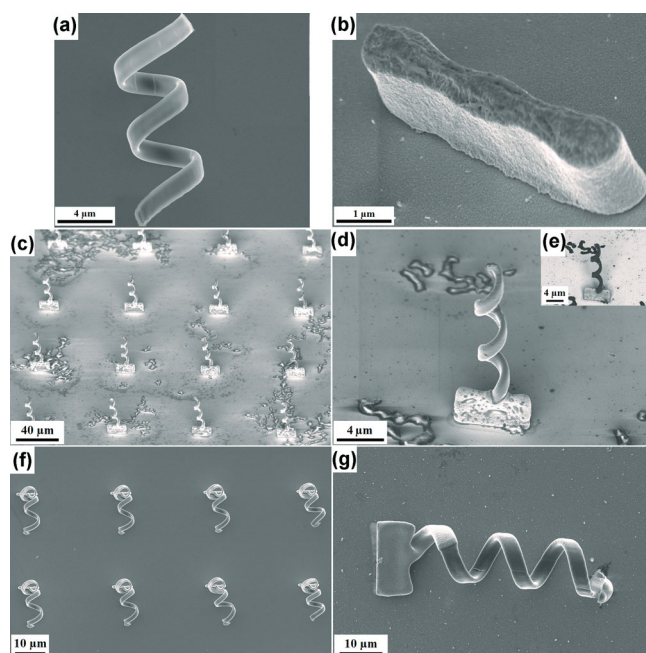
The DLW process parameters were systematically optimized. A laser power of 1.75 mW, a scan speed of 50 μm s^{-1} and a development time of 60 min in a developer concentration of 1:4 (AZ 400K : DI water) were found to be optimal to fabricate the 3D templates of Design A (**Figure 2**(a)) and Design B (Figure 2(c)). Figure 2(b) and (d) show FIB cross-sections of the template Design A and B, respectively. It is evident from these cross-sections that the channels reach the ITO layer and the channel diameter is uniform along the whole length.

Unlike vapor phase deposition methods, electrodeposition allows bottom-up filling of the templates with complex and narrow geometries. Due to the very special design of the 3D templates (featuring high aspect ratios, with lengths of up 66 μm and 0.65 μm in diameter), the electrodeposition process varies widely from planar (conventional) electrodeposition and, therefore, the electrodeposition conditions must be carefully selected. There are various requirements to achieve complete filling of 10 μm to 20 μm templates/channels, such as wetting of the templates, appropriate deposition rates to avoid hydrogen evolution at the cathode and, hence, porosity, and a very high chemical/mechanical stability of the templates in electrolytic environments. Pulsed electrodeposition (PED) was the method of choice for deposition of CoNi heads to ensure the growth of a fine crystalline deposit. A wetting step prior to electrodeposition is vital for obtaining uniform deposits inside the 3D templates (see Figure S3.1). The helical PPy tail was subsequently deposited onto the CoNi head by direct current (DC) electrodeposition (**Figure 3**(a)). The filament has a thickness of 1.6 μm along the helix axis and 0.65 μm perpendicular to the helix axis. The filament dimensions are consistent with the template design confirming a complete filling
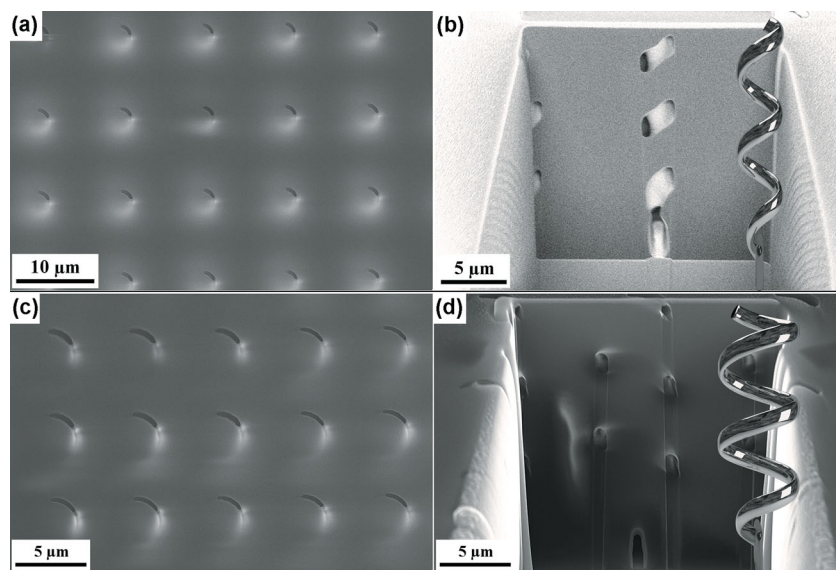
Figure 2. Photoresist templates of Design A and B before electrodeposition: (a) Top-view SEM image of A, (b) FIB cross-section of A with an illustration of the orientation of the to deposited h-ABF, (c) and (d) are the corresponding images for Design B.
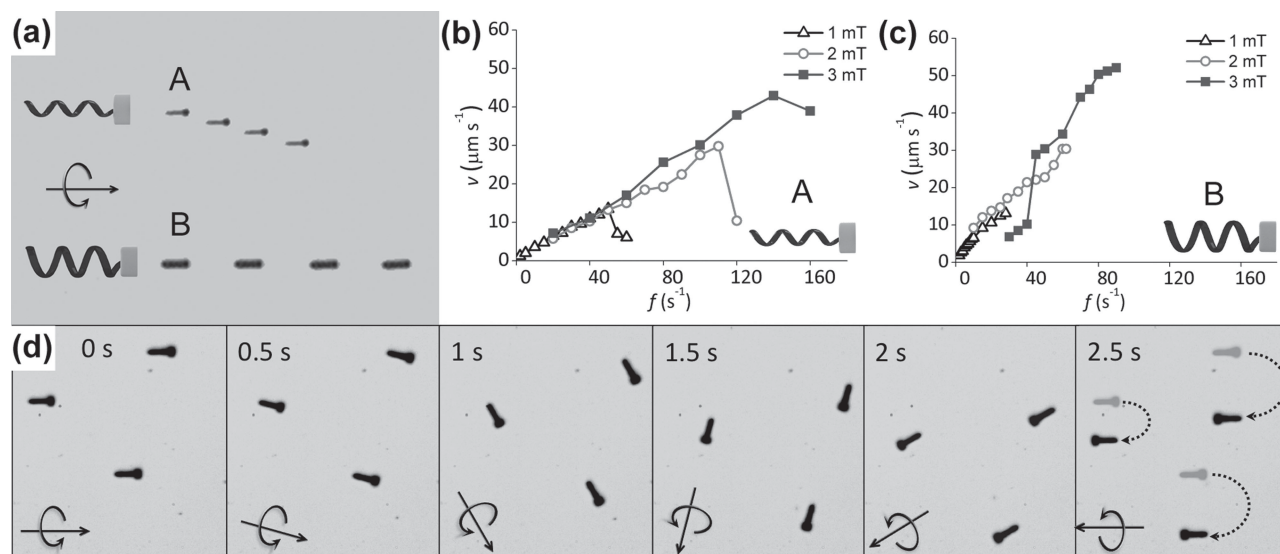
Figure 3. SEM images of h-ABFs after photoresist removal: (a) Helical tail consisting of PPy (Design B), (b) CoNi head, (c) array of h-ABFs of Design A, (d) single h-ABF of Design A, (e) corresponding BSE image, (f) array of h-ABFs of Design B, (g) single h-ABF of Design B.

SEM image of a single CoNi head achieved by electrodeposition. The microstructure of CoNi is smooth with no evident pores. The PED condition resulted in a horizontally aligned filling of the channels with CoNi, meaning that the front of growing deposits always lays parallel to the working electrode surface. Both ends of the head are thicker than rest of the structure, which can be attributed to the higher concentration of the electrical field lines at the edges.

Figure 3(c) and (f) show arrays of vertically standing h-ABFs corresponding to Design A and Design B, respectively. It can also be observed that filling of the templates was homogeneous and therefore, all h-ABFs have equal dimensions. Additionally, the connection of the different segments (CoNi head + PPy tail) is strong and remains intact after removal of the resist. Due to the smaller helix diameter of Design A, all h-ABFs stood upright, while the PPy tail of Design B, which is much heavier and less rigid due to its design, caused it to bend close to the connection to the head segment. It is evident that deposited PPy is flexible. Figure 3(d), (g) shows magnified SEM images of the same samples. The inset (e) in Figure 3(d) shows the same h-ABF imaged with a back-scattered electrons (BSE) detector. The bright appearance of the head segment is related to the strong electron backscattering of the heavy Co and Ni elements. The PPy consists of lighter elements and appears darker. An elemental analysis by EDX was performed by spot measurements at both segments of the hybrid 3D structures. The analysis confirmed a composition of 37% Co and 63% Ni for the head segment (see Table S4.1). The analysis of the tail shows no Co or Ni contents, but contents of C, Na and S, which come from deposited PPy and sodium dodecylbenzenesulfonate (NaDBS) present in the electrolyte.

Figure 4 shows the velocity tests of h-ABFs with Design A and B. The forward velocity was recorded as a function of the input frequency of the rotating magnetic field and for

of the channels. The electrodeposited PPy helix shown in Figure 3(a) has a diameter of 4 μm and a pitch of 5.3 μm. The pitch of the helix is in accordance with the initial template design (Design B, 6 μm pitch), but the diameter was 2 μm smaller (actual helix diameter was 6 μm). The decrease in the diameter confirmed a shrinking of PPy after the resist was removed which might be related to residual stresses built up during growth or due to the PPy drying. Figure 3(b) is an

Figure 4. Magnetic manipulation of h-ABFs: (a) Time-lapse images of h-ABF forward motion at constant rotating frequency taken at 1.25 s intervals, (b) forward velocity v of Design A h-ABF plotted for different input frequencies f at magnetic fields strengths of 1, 2 and 3 mT, (c) corresponding plots for Design B, (d) swarm-like swimming of three h-ABFs. Images were captured at 0.5 s intervals while the rotational axis of the magnetic field was continuously turned.

field strengths from 1 to 3 mT (Figure 4(b) and (c)). The tests started at the lowest frequency that provided stable cork-screw motion (stabilizing frequency) and were stopped at frequencies where the velocity dropped significantly or motion became unstable, i.e, the step-out frequency (see Video S1 in Supporting Information). The stabilizing frequencies varied between 2 and 30 Hz depending on the field strength and the helix design. In the cork-screw motion regime, a linear increase of forward velocity with increasing input frequency was observed for both designs. The linear relation of velocity to input frequency recorded for Design B has a slope that is approximately twice as large as for Design A. The slope of the frequency-velocity curve represents the amount of forward displacement achieved for one rotation around the helical axis. This displacement is linearly related to the radius of the helix,[10] which explains the larger slope for Design B (see Video S2 in Supporting Information). The maximum velocity is not only function of the slope, but also a function of the step-out frequency. The step-out frequency is reached when the fluidic drag torque acting on the robot exceeds the available magnetic input torque. This point is influenced by the strength of the magnetic field and the geometry of the robot. The fluidic drag torque acting on the robot increases with the helix radius cubed, hence the step-out frequency decreases rapidly with growing helix radius. For a constant head size, the helical tail design, therefore, represents a compromise between maximizing the forward displacement per rotation (large helix radius) and minimizing the fluidic drag torque (small helix radius). Figure 4(b) and 4(c) show that it is possible to achieve the same maximum velocity (i.e. the same "compromise") with two different tail designs. The influence of the different shape parameters on the propulsion has been presented in previous publications.[4,10]

Three microagents were manipulated to demonstrate a swarm-like behavior in a controlled fashion, as can be seen in Figure 4(d) and Video S3 in Supporting Information. While a swarm of microagents of equal design can be controlled as a single entity, swarms of microagents of different designs (sizes and shapes) can be used to single out individual microagents due to the frequency dependence of the propulsion. This was successfully shown by Peyer et al.[4]

Experimental Section

Fabrication of 3D Templates: After cleaning the glass substrates, a 25 nm thick ITO layer was deposited by the e-beam evaporation (UNIVEX 500, Leybold). Afterwards, samples were annealed at 550 °C for 5 min in a rapid thermal annealing oven (JetFirst100). AZ 9260 (MicroChemicals GmbH) was spin-coated on top of the ITO layer. A thickness of 20 μm was achieved by a two-step process, which allows a smooth and uniform resist layer. The first resist layer was spin-coated at 2400 rpm for 60 s followed by a soft bake at 110 °C for 100 s whilst the second layer was spin-coated at 1900 rpm for 60 s followed by a soft bake at 110 °C for 400 s. The 3D templates were written inside the resist by using DLW (Nanoscribe) system. After the exposure, the samples were developed for 60 min in AZ 400K developer (MicroChemicals).

Electrodeposition of CoNi Heads: The arrays of h-ABFs were obtained by a two-step electrodeposition process. The electrodeposition was carried out by a programmable potentiostat (Autolab PGSTAT302N, Ecochemie). Initially, ferromagnetic CoNi alloy head segments were electrodeposited by the PED (see supporting information S5.1). Cathodic pulses had a length of 4 ms whereas the intermediate rest phases of 10 ms were used at a current density of 50 mA cm^{-2}. A Ni sheet with dimensions of 2 cm × 10 cm was used as the counter electrode. An especially designed holder was used to immerse the 3D templates into the electrolyte. The electrolyte temperature was maintained at 55 °C. N$_2$ bubbling and constant stirring was used.

Electrodeposition of Polypyrrole Tail: The PPy tail segments were obtained by the electropolymerization of the pyrrole (see supporting information S5.2). A platinized Ti sheet of 2 cm × 2 cm was used as a counter electrode and the electrolyte was kept at the room temperature. The electrolyte was covered with a N$_2$ blanket to prevent from oxidation. The PPy electropolymerization was conducted by applying anodic DC current of 4 mA cm^{-2} to the working electrode. The resist was finally removed with acetone.

Wireless Actuation of Microagents: A small piece of the glass substrate containing the microagents was immersed in a reservoir made of PMMA (35 mm x 15 mm x 3 mm). The reservoir was filled with DI water and a clean Si substrate was placed next to the substrate to provide a smooth surface for the swimming tests. Afterwards, the reservoir was placed inside the manipulation Helmholtz coil-setup.[4] The detachment and placing of the microagents from the glass substrate to Si was carried out with a micromanipulator probe tip (T-4–22, Picoprobe). The motion of the microagents was observed and recorded with a light microscope equipped with a 480 × 640 pixel CCD camera (A602f, Basler).

Supporting Information

Supporting Information is available from the Wiley Online Library or from the author.

[1] B. J. Nelson, I. K. Kaliakatsos, J. J. Abbott, *Annu. Rev. Biomed. Eng.* **2010**, *12*, 1, 55.
[2] D. R. Frutiger, K. Vollmers, B. E. Kratochvil, B. J. Nelson, *Int. J. Robot. Res.* **2010**, *29*, 5, 613.
[3] L. Zhang, J. J. Abbott, L. Dong, B. E. Kratochvil, D. Bell, B. J. Nelson, *Appl. Phys. Lett.* **2009**, *94*, 6, 064107.
[4] K. E. Peyer, L. Zhang, B. J. Nelson, *Nanoscale* **2013**, *5*, 4, 1259.

[5] A. Gosh, P. Fischer, *Nanolett.* **2009**, *9*, 6, 2243.

[6] P. Fischer, A. Gosh, *Nanoscale* **2011**, *3*, 557.

[7] B. Rodenborn, C.-H. Chen, H. L. Swinney, B. Liu, H. P. Zhang. *Proc. Natl. Acad. Sci.* **2013**, *110*, 5, 1574.

[8] G. Zhao, M. Pumera, *Langmuir* **2013**, *29*, 7411.

[9] G. Zhao, A. Ambrosi, M. Pumera. *Nanoscale* **2013**, *5*, 1319.

[10] J. J. Abbott, K. E. Peyer, M. C. Lagomarsino, L. Zhang, L. Dong, I. K. Kaliakatsos, B. J. Nelson, *Int. J. Robot. Res.* **2009**, *28*, 11–12, 1434.

[11] S. Tottori, L. Zhang, F. Qiu, K. K. Krawczyk, A. Franco-Obregon, B. J. Nelson, *Adv. Mater.* **2012**, *24*, 6, 811.

[12] K. Vollmers, D. R. Frutiger, B. E. Kratochvil, B. J. Nelson. *Appl. Phys. Lett.* **2008**, *92*, 14, 144103.

[13] E. Smela, M. Kallenbach, J. Holdenried, *J. Microelectromec. Syst.* **1999**, *8*, 4, 373.

[14] K. M. Sivaraman, B. Özkale, O. Ergeneman, T. Lühmann, G. Fortunato, A. M. Zeeshan, B. J. Nelson, S. Pané, *Adv. Healthcare Mater.* **2013**, *2*, 4, 591.

[15] J. K. Gansel, M. Thiel, M. S. Rill, M. Decker, K. Bade, V. Saile, G. von Freymann, S. Linden, M. Wegener, *Science* **2009**, *325*, 5947, 1513.